ROYAL SOCIETY
OF CHEMISTRY

PAPER

Check for updates

Vertical numbering-up microfluidic architecture for scalable and homogeneous lipid nanoparticle production

Zhaoyu Zhang,†[a] Jaejeung Kim, iD †[ab] Jinwoo Hwang,[a] Hyunjo Seo,[a] Geonha Kim,[a] Seoyeon Choi, iD [ab] Kyung-A Hyun iD [c] and Hyo-ll Jung iD *[abd]

Lipid nanoparticles (LNPs) are a key platform for nucleic acid delivery, but their industrial-scale production remains a critical bottleneck. While microfluidics ensures high-quality LNP production, conventional single layer strategies suffer from low throughput. Existing scaling strategies, like parallel or 3D devices, face limitations in flow distribution and fabrication complexity, failing to balance throughput with LNP quality. Here, we report a robust, vertically stacked microfluidic cartridge (VeSMiC) fabricated using polycarbonate (PC) that successfully addresses the flow distribution challenge. This platform integrates a hydrodynamic tapered inlet structure, ensuring uniform flow partitioning across layers, with re-Tesla mixers for rapid synthesis. A five-layer device was scalably fabricated using a two-step surface modification and a robust bonding method. This device enabled stable operation at a high total flow rate (0.96 L per hour) operation and increased LNP throughput 7-fold compared to a single channel. Critically, this high throughput did not compromise quality; LNPs consistently maintained an average size of 100–150 nm, a low polydispersity index (PDI) below 0.12, and high encapsulation efficiency above 96%. Furthermore, they also demonstrated significant therapeutic efficacy in an *in vitro* wound model. Notably, an 80-cartridge platform is projected to achieve a production flow rate of approximately 80 L per hour, validating this platform as a viable solution for industrial-scale LNP manufacturing.

1. Introduction

Lipid nanoparticles (LNPs) are versatile lipid-based carriers engineered for the precise and controlled delivery of therapeutic cargoes.[1–3] Positioned at the intersection of nanotechnology and medicine, LNPs provide clear advantages for drug and vaccine development.[4] These advantages stem from their inherent biocompatibility due to membrane similarity, high payload potency, tuneable particle size and surface chemistry.[5–7] Currently, LNPs have demonstrated significant promise in nucleic acid-based therapeutic for anti-tumour, anti-fibrotic, and anti-inflammatory applications in preclinical and early-stage clinical studies.[8–10] Among techniques employed for LNP production, microfluidic mixing technology offers superior controllability,[11–13] enabling precise sizing and continuous processing with narrow

polydispersity, thereby being widely recognized as the most promising strategy for LNP production.[14–16] Based on this, we previously reported a reverse-Tesla (re-Tesla) valve structured microfluidic chip with high mixing efficiency to continuously produce lipid-based nanoparticles.[17] Specifically, this geometry maximizes mixing efficiency through collision-based transverse impingement derived from the reverse flow principle, enabling high-quality LNP synthesis. However, LNP production based on single-channel designs is constrained by channel dimensions; these systems typically operate in confined microchannels at low volumetric throughput resulting in limited flow rates and restricting their application to small-scale studies.[18,19] Thus, while the global demand for LNP-based medicines continues to increase, robust and scalable manufacturing remains a bottleneck.[20,21] Therefore, the development of microfluidic-based LNP mass production technologies is essential to accelerate the clinical translation and widespread adoption of nucleic acid therapeutics.[22,23]

A variety of strategies have been explored to increase the throughput of LNPs to achieve the production flow rates (approx. 0.8–3.6 L per hour) necessary for formulation optimization and pilot-scale studies toward commercialization,[24,25] including parallel multi-channel operation,[26,27] vortex fluid focusing,[28,29] and axial stream

[a] *School of Mechanical Engineering, Yonsei University, 50 Yonsei-ro, Seoul, South Korea. E-mail: uridle7@yonsei.ac.kr*

[b] *The DABOM Inc., 50 Yonsei-ro, Seoul, South Korea*

[c] *School of Biopharmaceutical and Medical Sciences, Sungshin Women's University, 55 Dobong-ro, Seoul, South Korea*

[d] *Department of Integrated Medicine, Yonsei University, 50 Yonsei-ro, Seoul, South Korea*

† These authors contributed equally to this manuscript.

convergence.[30,31] However, fundamental constraints have limited existing designs to incremental gains in throughput, hindering the transition to large-scale production. These constraints include significant manufacturability challenges, such as the complex fabrication of 3D channel geometries required for certain mixing strategies. Furthermore, major scalability bottlenecks arise during parallelization,[32,33] where ensuring uniform flow distribution and consistent pressure drops across numerous parallel channels is notoriously difficult. This often leads to poor flow-rate reproducibility, compromising the consistency of LNP key quality attributes (KQAs). Consequently, there is a pressing need for a novel microfluidic system that can achieve stable and sustain operation at high flow rates and elevated pressures, while ensuring the KQAs of LNPs during high-throughput synthesis.[34,35]

Herein, we developed a scalable high-throughput microfluidic platform that employs a vertically stacked architecture and is inherently expandable through horizontal parallelization.[35] We first demonstrated a single layer microfluidic chip that incorporates a re-Tesla valve structure and is fabricated from polycarbonate (PC) using computer numerical control (CNC) machining, which achieves mixing efficiency above 95% (Fig. 1A). To elevate the production rate beyond the limitations of a single layer chip, we increased the number of production units by vertically stacking the identical chips. This design maximized production density within higher space utilization, resulting in a newly designed device termed the vertically stacked microfluidic cartridge (VeSMiC). To ensure uniform flow distribution across all layers, the VeSMiC incorporated a tapered inlet design that balanced hydraulic resistance, enabling predictable fluidic control within a compact device. It preserved the performance of the single layer chip while substantially increasing production throughput (Fig. 1B). Finally, the modularity platform supported scalability in multiple dimensions, allowing additional throughput gains through large-scale parallel integration. Based on a theoretical model, the horizontal parallelization of multiple VeSMiCs could achieve order-of-magnitude throughput improvements (Fig. 1C). Collectively, these features established a robust and scalable platform for high-throughput LNP synthesis, delivering maximized efficiency and significant savings in time and cost, all within a compact device architecture.

2. Methods and materials

2.1 Materials

PC substrates and PC films (Makrofol®) were purchased from Covestro (Germany). Waterproof pressure-sensitive adhesive (PSA) tape (VHB™) was purchased from 3M (USA). Anhydrous ethanol, sodium acetate, phosphate-buffered saline (PBS),
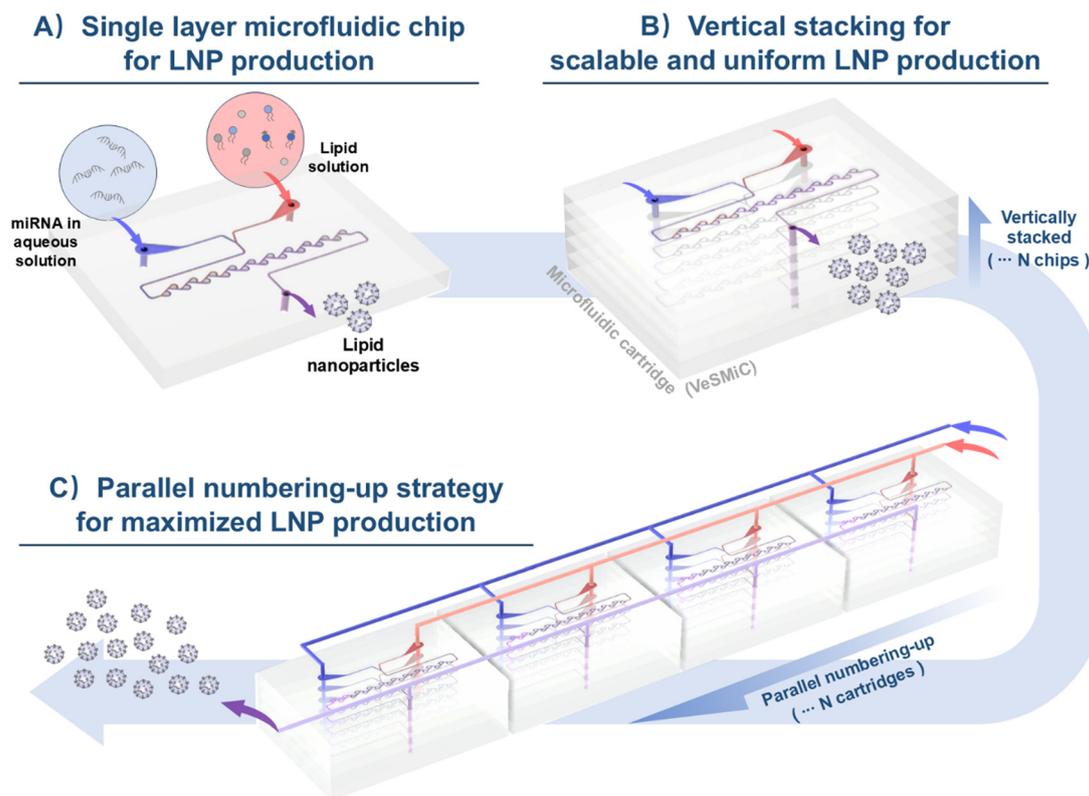
Fig. 1 (A) A single layer microfluidic chip with re-Tesla valves performs sub-millisecond mixing to yield clinical-grade LNPs. (B) A multi-layer VeSMiC ensures uniform interlayer flow, while leak-free bonding forms a robust 3D channel network. (C) A potential scalable LNP production platform based on VeSMiC and its parallelization, enabling order-of-magnitude production rate scaling.

bovine serum albumin (BSA), fluorescent beads, polyethylene glycol (PEG-2000), Triton™ X-100, and all buffer reagents were obtained from Sigma-Aldrich (USA). The ionizable lipid DLin-MC3-DMA was obtained from MedChem Express (MCE, China), while 1,2-distearoyl-*sn*-glycero-3-phosphocholine (DSPC), cholesterol, and DMG-PEG 2000 were purchased from Avanti Polar Lipids (USA).

2.2 Modelling of computational flow dynamics in microfluidic channels

The design of the microfluidic chip was adapted from a previously reported re-Tesla structure.[17] The fluid dynamics was modelled using COMSOL Multiphysics software, by solving the Navier–Stokes and convection–diffusion equations. The model employed a single-phase fluid with properties of a water–ethanol mixture (ρ = 970 kg m^{-3}, μ = 1.8 mPa s).[36] Boundary conditions included experimental flow rates at the inlets, zero pressure at the outlet, and no-slip walls and the results were confirmed to be mesh independent.

2.3 Fabrication and evaluation of single layer microfluidic chips

The microfluidic chip was fabricated on PC substrates using a CNC micromachining system (Kangintech, South Korea). The channels were designed to be 500 μm in width and 200 μm in height, with toolpaths generated in Autodesk Inventor CAM. The fabrication process began by boring the inlet/outlet ports using a 1 mm flat end mill (5000 rpm spindle speed, 1000 mm min^{-1} feed rate). Subsequently, the microchannels were machined using a 0.4 mm flat end mill (18 000 rpm, 400 mm min^{-1} feed rate) with a multiple-depth strategy to ensure precision.

To render the channel surface hydrophilic, the PC substrates were treated with oxygen plasma followed by PEG adsorption.[37–39] Detailed fabrication and surface treatment procedures are described in SI 2.3.1.

The performance of mixing effects in microfluidic chips was validated through fluorescence imaging experiments using a 1 : 100 mixture of 0.1 μm fluorescent beads and BSA as tracer reagents. Flow behavior was monitored with a fluorescence microscope, and the images were analyzed with ImageJ (NIH, USA) to obtain fluorescence intensity distributions. The standard deviation for calculating the mixing efficiency was calculated as follows:

$$\sigma = \sqrt{1/N \sum_{I=1}^{N} (I_i - \bar{I})^2}$$

where N denotes the number of pixels in the mixing area, I_i represents a local pixel intensity value, and $\bar{I}$ signifies the pixel intensity value for optimal mixing.[40] The mixing efficiency was then calculated according to the following equation:

$$\text{Mixing efficiency} = 1 - \sigma_n/\sigma_{\max}$$

where σ_n is the standard deviation of the pixel intensities for n selected parts and $\sigma_{\max}$ is the maximum standard deviation.

2.4 Assembly of VeSMiC

After drying the individual surface treated chip layers, each layer's channels were sealed with a pre-perforated PC film that functions as a fluidic access layer. Pre-perforated PSA tape was subsequently applied over the PC film to serve as the interlayer bonding agent and waterproof seal for vertical stacking. The assembly was conducted sequentially by aligning and bonding a PSA tape-laminated upper chip to a lower chip using CNC-machined positioning holes, repeating the process to reach the desired layer count. The entire stack was then mechanically secured with screws to ensure structural integrity and prevent leakage at high total flow rates (TFRs), defined as the sum of the flow rates of the lipid and aqueous phases.

2.5 Synthesis of LNPs

The lipid phase was prepared by dissolving DLin-MC3-DMA, DSPC, cholesterol, and DMG-PEG 2000 in ethanol at a molar ratio of 50 : 10 : 38.5 : 1.5 to a final lipid concentration of 1 mg mL^{-1}. The lipid mixture was vortexed and gently sonicated at room temperature until fully dissolved as a clear and homogeneous solution.[41] The aqueous phase consisted of hsa-miR-3162 (Bioneer, South Korea) dissolved in 100 mM sodium acetate buffer (pH 4.5) at a nitrogen-to-phosphate (N/P) ratio of 6.[42] The lipid and aqueous phases were mixed within the microfluidic chips at a flow rate ratio (FRR) of 3, defined as the ratio of the flow rates of the lipid solution to those of the aqueous buffer. The collected LNP samples were purified and subjected to buffer exchange into PBS buffer (pH 7.0) using a 100 kDa MWCO membrane for subsequent experiments.

2.6 Characterization of LNPs

The average size and polydispersity index (PDI) of the LNPs were determined by dynamic light scattering (DLS, Zetasizer Nano ZS, Malvern Panalytical, UK) and the production rate was quantified by nanoparticle tracking analysis (NTA, Nanosight LM10, Malvern Panalytical, UK). The encapsulation efficiency (EE%) of miRNA was measured using the RiboGreen Assay and was calculated using the following equation:

$$\text{EE (\%)} = \frac{\phi p - \phi a}{\phi p} \times 100$$

where ϕp and ϕa indicate the fluorescence intensities measured in the presence and absence of 1% (w/v) Triton X-100, corresponding to the amount of total and unencapsulated miRNA, respectively.

2.7 *In vitro* evaluation of cytotoxicity and therapeutic effects

The cytotoxicity of LNP formulations was assessed on HaCaT cells, purchased from ATCC, using a CCK-8 assay (GlpBio, USA). Cells were cultured at a density of 1×10^4 cells per well and incubated for 24 h, then followed by treatment with a fresh medium containing various concentrations of LNP formulations for an additional 24 h. After a 1 h incubation with the CCK-8 reagent, absorbance was measured using a microplate reader to determine cell viability. Cell viability was calculated using the following equation:

$$\text{Cell viability (\%)} = \frac{(\text{Ab}_s - \text{Ab}_b)}{(\text{Ab}_c - \text{Ab}_b)} \times 100$$

where Ab_s, Ab_c, and Ab_b represent the absorbance of the sample, control, and blank wells, respectively.

The cell migration was evaluated *via* a scratch wound healing assay. HaCaT cells were cultured until >90% confluence. A uniform scratch was created in the cell monolayer, which was then treated with a medium containing either PBS (control), LNPs produced by a single layer chip, or LNPs from tapered inlet structure VeSMiC. Wound closure was imaged at 0 h and 12 h, and quantified using ImageJ software and the wound closure rate was calculated according to the following formula:

$$\text{Wound closure rate (\%)} = \frac{(A_{0h} - A_i)}{A_{0h}} \times 100$$

where A_{0h} is the initial scratch area at 0 h and A_i is the scratch area at the subsequent time point.

2.8 Fabrication and evaluation of the scalable platform

The achievable scaling efficiency of the vertical numbering-up scalable platform was predicted using a theoretical model. The throughput-to-flow ratio (k) was defined as the ratio of the throughput (P_{single}) to the TFR (Q_{single}) of a single layer chip:

$$k = \frac{P_{\text{single}}}{Q_{\text{single}}}$$

A correction factor (ψ) was introduced to account for fluid retention, where P_{unit} and Q_{unit} are the production rates and TFR of a single VeSMiC:

$$\psi = \frac{P_{\text{unit}} / \left(5 \times P_{\text{single}}\right)}{Q_{\text{unit}} / \left(5 \times Q_{\text{single}}\right)}$$

The total production rates of an N-cartridge platform (P_N) were calculated as:

$$P_N = k \times \psi \times (NQ_{\text{unit}})$$

And the achievable scaling efficiency (E_N) relative to a single layer chip was calculated as:

$$E_N = \frac{P_N}{P_{\text{single}}} \times 100\%$$

2.9 Statistical analysis

All experiments were performed as three independent trials ($n = 3$), and statistical analyses were performed using GraphPad Prism 10 software (GraphPad, La Jolla, CA); the results were presented as the mean ± standard deviation (SD). One way ANOVA was used to evaluate the statistical significance of differences between two groups. The significance level was set at 0.05 for the p-value; *$p < 0.05$, **$p < 0.01$, and ***$p < 0.001$ were used to indicate significant differences, while N.S. indicates no significant difference ($p > 0.05$).

3. Results and discussion

3.1 Design of the single layer PC re-Tesla microfluidic chip

Scalable production of LNPs requires microfluidic systems that can reliably achieve high mixing efficiency under conditions with large-volume operation. Building on our previous work using the re-Tesla structure for nanoparticle synthesis,[17] we assessed the performance of a single layer re-Tesla chip fabricated using PC as the fundamental unit of our scalable platform (Fig. 2A). In contrast to previously reported PDMS-based devices, a channel width of 500 μm was selected to balance the precision limits of CNC fabrication with the demands of high mixing effects. To ensure efficient mixing operation, the re-Tesla microfluidic chip was designed to maintain the pressure drop below the normal operating pressure limit (<310 kPa) for microfluidic systems.[43] Based on this principle, we assessed the impact of the number of re-Tesla cycles and the total flow rate (TFR) on the pressure drop. Here, as shown in Fig. 2A, a re-Tesla cycle is defined as a paired upper and lower mixing part arranged sequentially along the flow direction.[44] All experiments were conducted at a flow rate ratio (FRR) of 3, which has been reported to be optimal for pump-driven LNP formulations.[45,46] While maintaining chip compactness comparable to conventional PDMS chips, we first established the upper limit of the number of re-Tesla cycles to 12 numerical simulations and were used to analyse the pressure drop across the channel depending on TFRs. The results indicated that at TFRs of 6 mL min⁻¹ and above, the pressure drop exceeded the 310 kPa limit even at a low number of cycles (Fig. 2B). However, a low number of cycles may induce insufficient mixing within the channel, which likely causes instability in the produced particles. Therefore, a TFR of 4 mL min⁻¹ was selected as the maximum TFR for the single layer chip to ensure stable operation without exceeding the pressure limit.

We then analysed the mixing effect at a set number of cycles and TFR using CFD simulations (Fig. 2C) and fluorescence imaging (Fig. 2D). The simulation results revealed a mixing efficiency of approximately 96.3% in ten cycles and increased slightly to 97.7% in twelve cycles. Also, this trend was corroborated by fluorescence images, showing
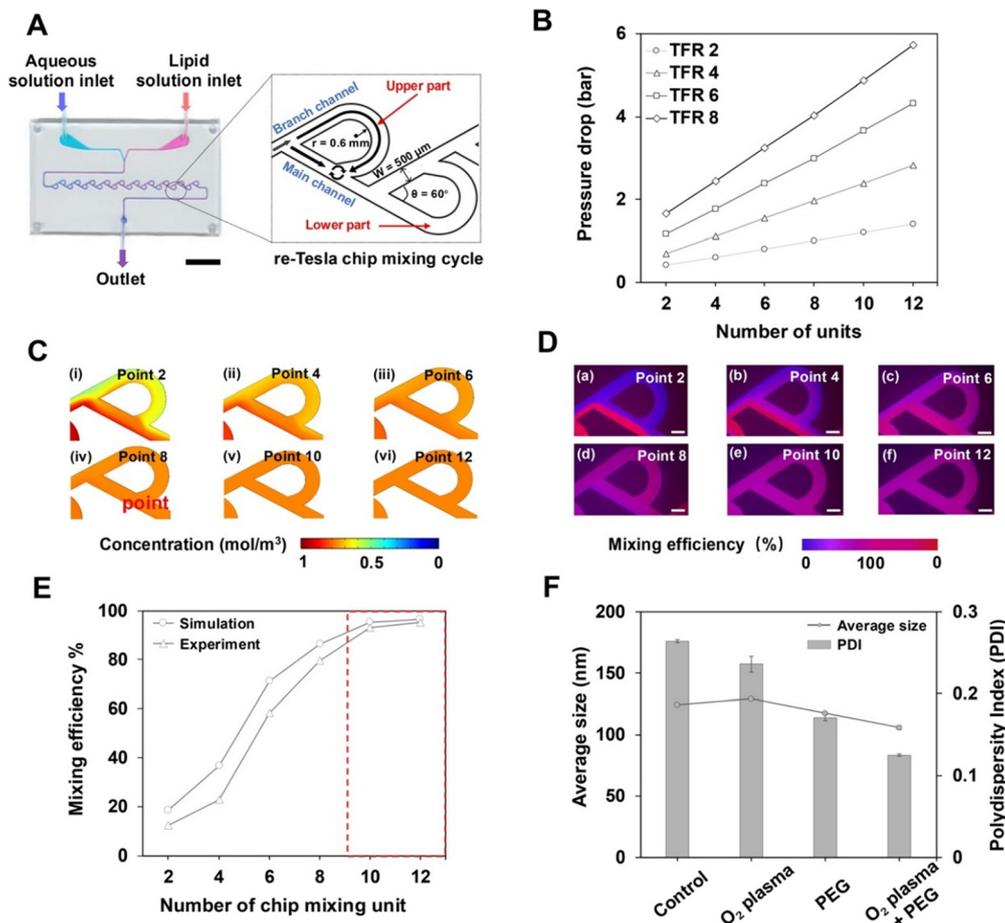
Fig. 2 (A) Schematic of the re-Tesla valve that promotes mixing behaviour in a single layer chip. (B) Total pressure drop of the re-Tesla channel with 12 sequential mixing cycles under varying TFR conditions. (C) Performance of simulated mixing as a function of the number of mixing cycles in a 12-cycle re-Tesla channel. (D) Performance of mixing depending on the number of mixing cycles and analysed by fluorescence imaging. (E) Comparison of fluorescence imaging experimental and simulated mixing performance. (F) Comparative characterization of LNPs produced in chips subjected to different surface treatments.

comparable efficiencies of 95.2% and 96.2%, respectively (Fig. 2E). Therefore, for the effective mixing at a low-pressure drop while maintaining compact channel geometry for high fidelity, a ten-cycle channel was chosen as the final design for the standard microfluidic chip.

Finally, we aimed to address the challenges associated with the native PC surface, including its limited wettability that could cause bubble adhesion during operation. These effects can interfere with rapid solvent exchange and controlled nucleation during self-assembly of nanoparticles, resulting in larger and less uniform nanoparticles.[47,48] We therefore explored four surface modification strategies to simultaneously enhance hydrophilicity and improve LNP synthesis quality (Fig. S1). For the four strategies, the chip was treated simultaneously with oxygen plasma and PEG minimized bubble formation during operation. Also, it produced the smallest LNPs with excellent size uniformity (PDI < 0.2) that could be beneficial for facilitating the transport of therapeutic payloads, such as miRNA, through cell membranes (Fig. 2F). The surface coating was maintained for at least 7 days, resulting in stable and reproducible LNP

formation (Fig. S2). In addition, the formation of larger LNPs with maintained size uniformity at low TFRs verified that stable and size-controlled LNP synthesis could be achieved using the PC single layer chip (Fig. S3).

3.2 Design of the inlet structure for uniform flow distribution in VeSMiC

The vertically stacked microfluidic cartridge (VeSMiC), featuring a highly space-efficient scaling strategy by layering single layer chips, enables high-throughput production. However, a critical challenge in scaling-up production through this architecture lies in maintaining uniform flow distribution across all chip layers to ensure consistent LNP quality. This fluid dynamic behavior can be interpreted analogously to Kirchhoff's current law,[49,50] where pressure losses in the inlet supply line lead to severe maldistribution of flow into the inlet lateral line.

To address this, we modified the inlet structure of the VeSMiC to compensate for the pressure recovery, which leads to a non-uniform pressure distribution in the flow

supply line manifold. Maintaining uniform flow resistance across all inlet supply lines is critical for achieving consistent flow rates through each parallel channel. This can be evaluated using the relationship between the pressure drop ΔP and the flow resistance R_f at the inlet of the n-th layer expressed as:[51]

$$\Delta P_n = nQR_{\mathrm{f},1} = n\Delta P_1$$

where $n = 1$ corresponds to the top layer closest to the inlet, and numbering proceeds downwards to the bottom layer. According to the Hagen–Poiseuille equation, the pressure drop within each inlet supply line is given by:

$$\Delta P_n = \frac{8\eta L}{\pi r_n{}^4} Q_n$$

where L is the length (thickness) of each layer in the inlet supply line, r_n is the radius of the inlet supply line at the n-th layer, and η is the dynamic viscosity of the fluid.

Therefore, by adjusting the inlet radius r_n according to the pressure drop, the flow resistance of each layer can be balanced, ensuring uniform volumetric flow across all channels. The inlet radius can be expressed as:
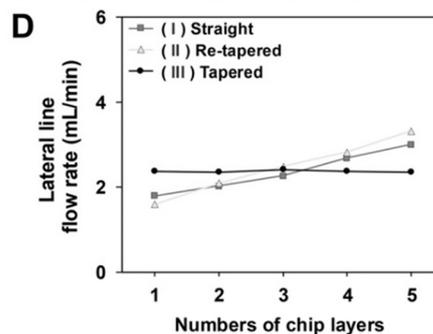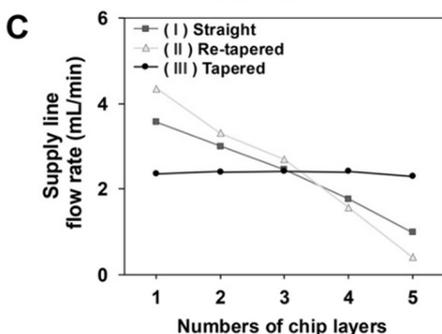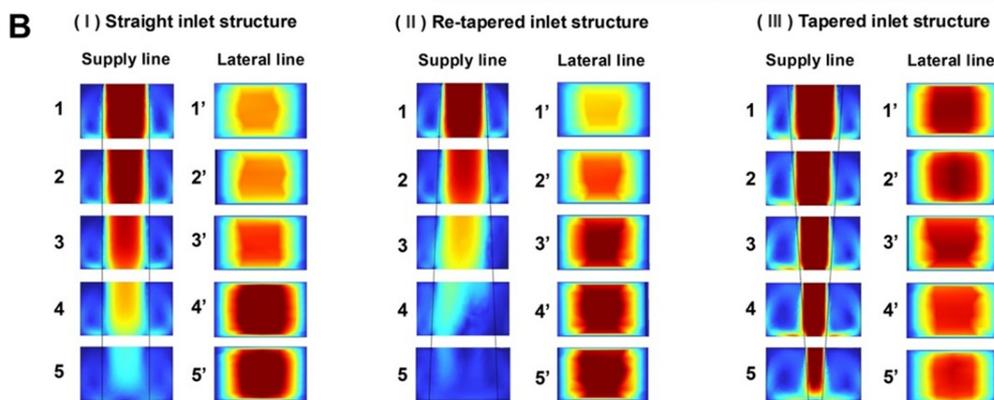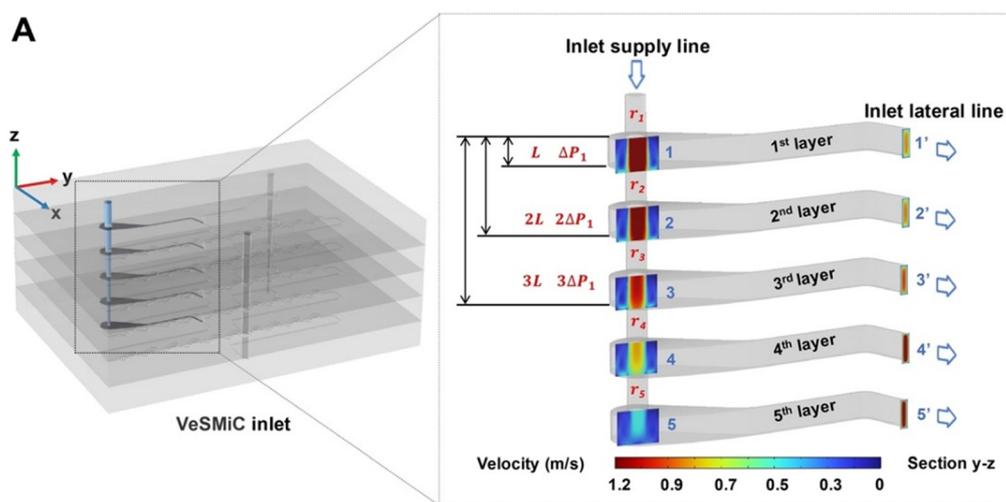

Fig. 3 (A) Schematic of inlet structure formed by vertically stacked configurations. (B) Simulated velocity fields in the inlet supply and lateral lines for the three inlet structures: (I) straight inlet structure, (II) re-tapered inlet structure, (III) tapered inlet structure. CFD-simulated distribution of layer-specific flow rate in (C) the inlet supply line and (D) the inlet lateral line.

$$r_n = r_1 \left(\frac{\Delta P_1}{\Delta P_n} \right)^{\frac{1}{4}} = r_1 n^{-\frac{1}{4}}$$

where r_1 is the radius of the inlet supply line at the first layer of the VeSMiC.

Based on the derived relationship, a tapered inlet structure featuring progressively decreasing inlet diameter was identified as the most suitable design to achieve uniform flow distribution across the stacked layers. This structure is specifically designed to counteract the pressure recovery within the vertically structured inlet supply line, a phenomenon where static pressure increases in the bottom layers (Fig. 3A). By systematically decreasing the radius r_n, we introduce progressively higher fluidic resistance R_f to the inlet lateral line of these distal layers, thereby balancing the flow distribution.

To validate the efficacy of the tapered inlet structure, we then performed a comparative computational fluid dynamics (CFD) simulation (Fig. 3B). This simulation compared the tapered inlet structure with two control structures—a straight inlet with a constant diameter and a reverse-tapered inlet with an increasing diameter—representing the uncompensated and overcompensated flow conditions, respectively. The total flow rate was set to 12 mL min^{-1}, which corresponds to the maximum operating condition under which all inlet designs remain within the system pressure constraint (<310 kPa) (Fig. S4). To maintain experimental continuity, the diameter of the inlet supply line for each structure from the 1st layer was established to be consistent with the tubing (1.52 mm) utilized in prior PDMS-based apparatus. This value served as the baseline for diameters of the inlet supply line for each structure summarized in Table 1.

The straight and re-tapered inlet structures both caused severe pressure maldistribution in the inlet supply line. This was reflected in the velocity distribution plots and quantitative outlet flow data for the inlet supply line (Fig. 3C) and the inlet lateral line (Fig. 3D). The results indicated insufficient flow into the top layer lateral line, with most of the fluid being diverted to the bottom layers of the stack. In stark contrast, the tapered inlet structure, by systematically reducing the cross-sectional area of the inlet supply line, effectively compensated for the cumulative hydraulic resistance. This maintained a nearly uniform velocity distribution throughout the inlet supply line, resulting in almost identical flow rates of the inlet lateral line across all five layers. These findings confirm that the tapered inlet

structure provides high flow uniformity and balanced pressure distribution over other inlet structures, ensuring consistent and layer-independent nanoparticle synthesis in the high-throughput VeSMiC.

3.3 Performance and biological validation of the VeSMiC

To construct a vertically stacked device capable of high flow-rate operation, a robust bonding method that preserves microchannel integrity is essential. We evaluated three assembly strategies: bolted fixation, PDMS film lamination, and a biocompatible PSA tape interlayer (Fig. S5). Leakage tests demonstrated the superior performance of the PSA tape interlayer, which withstood TFRs up to 16–18 mL min^{-1}, whereas the bolted fixation and PDMS film lamination chips failed at approximately 3 mL min^{-1} and 10 mL min^{-1}, respectively (Fig. 4A). An ink perfusion test further confirmed the fluidic integrity and uniform mixing capability of the PSA tape-bonded chip (Fig. 4B). Using this optimized bonding technique, we fabricated VeSMiC with three distinct inlet structures (Fig. 4C) and systematically evaluated their LNP production performance across a TFR range of 4 to 16 mL min^{-1}, a range that ensures sufficient residence time for effective chaotic mixing at each layer[47,52] (Table S1). This range was established with the single layer chip optimal TFR as the starting benchmark and an upper limit set to provide a conservative margin for long-term operational stability.

The straight and re-tapered structures exhibited reduction in monodispersity with increasing flow rates. This polydispersity is a direct consequence of the severe pressure maldistribution inherent in these inlets, which leads to significant flow rate non-uniformity across the parallel layers. This results in inconsistent mixing conditions, yielding a heterogeneous particle population with reduced uniformity and uncontrolled particle growth (up to 194 nm). In sharp contrast, the tapered inlet VeSMiC achieved hydrodynamic balance, ensuring uniform flow distribution across all layers. This enabled consistent, layer-independent nanoparticle synthesis, allowing it to consistently produce highly monodispersed LNPs. This superior production robustness was demonstrated by its TFR-dependent controllability, in sharp contrast to the uncontrolled particle growth seen in the other structures; the tapered inlet structure VeSMiC offered predictable size modulation, exhibiting a 58 nm decrease in particle size as the TFR increased from 4 to 16 mL min^{-1} (Fig. 4D). Crucially, this modulation was achieved

Table 1 Diameter of the inlet supply line with varying inlet structures (inferred from the radius)

|	(I) Straight structure (mm)	(II) Re-tapered structure (mm)	(III) Tapered structure (mm)
1st layer	1.52	1.52	1.52
2nd layer	1.52	1.81	1.28
3rd layer	1.52	2.00	1.16
4th layer	1.52	2.15	1.08
5th layer	1.52	2.27	1.02
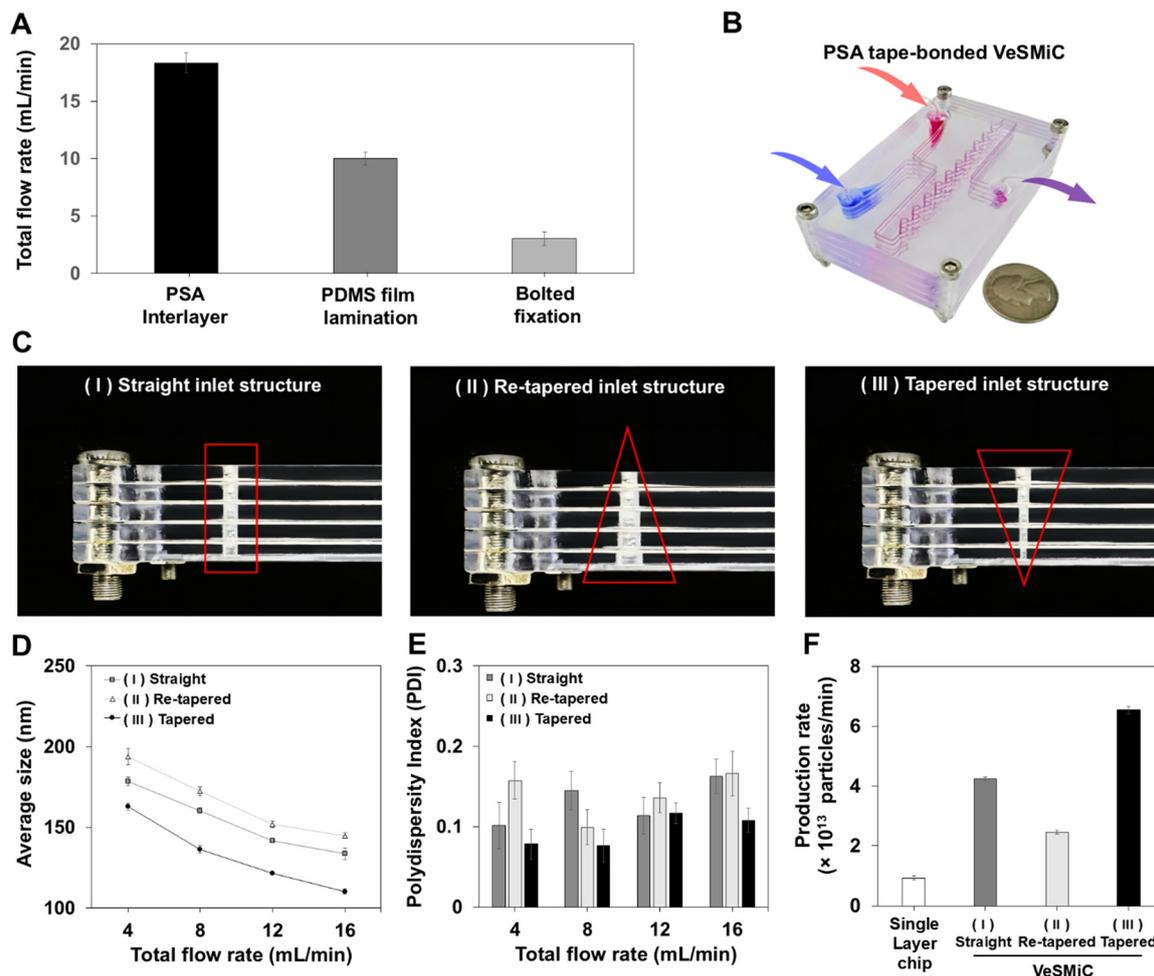
Fig. 4 (A) Results of the leakage experiment showing the maximum tolerable TFR for VeSMiC assembled with three different bonding strategies. (B) Dual-color ink perfusion test demonstrating the fluidic integrity and uniform distribution. (C) Schematic of the three inlet structures of the VeSMiC assembly using the PSA tape interlayer method: (I) straight inlet structure VeSMiC, (II) re-tapered inlet structure VeSMiC, and (III) tapered inlet structure VeSMiC. (D) Average size of LNPs produced by the three inlet structures of VeSMiC as a function of TFR. (E) Comparison of PDI distributions for LNPs generated with three different inlet structures of VeSMiC across a range of TFRs. (F) Comparison of maximum production rate performance between three different inlet structures of VeSMiC and single layer chips.

while simultaneously maintaining a stable PDI below 0.12, which was particularly evident at the maximum TFR (Fig. 4E). This demonstrated the ability to sustain LNP quality at high flow rates directly translated to a significant increase in production throughput. At its optimal TFR of 16 mL min^{-1} (defined by average size, PDI), the tapered inlet structure VeSMiC achieved a production rate of 6.5×10^{13} particles per min (Fig. 4F), representing a 7-fold increase over a single layer chip operating at 4 mL min^{-1}.

Critically, this enhanced throughput was achieved without compromising the encapsulation effect of nucleic acids (Fig. 5A), which remained above 96% and was comparable to the performance of the single layer device at its optimized flow rate. Prior to comparing the therapeutic effects of LNPs produced by each microfluidic device, we evaluated their cytotoxicity in HaCaT cells. A CCK-8 assay was performed after incubating HaCaT cells for 24 hours with five different concentrations of the

LNPs (Fig. 5B). The results showed that both LNP groups, produced by the single layer chip and the tapered inlet structure VeSMiC, exhibited no significant cytotoxicity, even when treated at doses up to 1×10^7 particles. Following the validation of the device's physical production performance, we next evaluated the biological functionality of the produced LNPs. We assessed the therapeutic potential of miRNA-loaded LNPs using an *in vitro* wound healing assay (Fig. 5C). As shown in Fig. 5D, after 12 hours of treatment with miRNA-loaded LNPs at a dose of 1×10^8 particles, those prepared using the single layer chip and the tapered inlet structure VeSMiC exhibited wound closure rates of 94.3% and 98.3%, respectively, demonstrating significant therapeutic efficacy compared to the control group (30.9%). These results indicate that the LNPs produced by the VeSMiC not only have high yield and uniform quality, but also successfully encapsulate bioactive miRNA, demonstrating
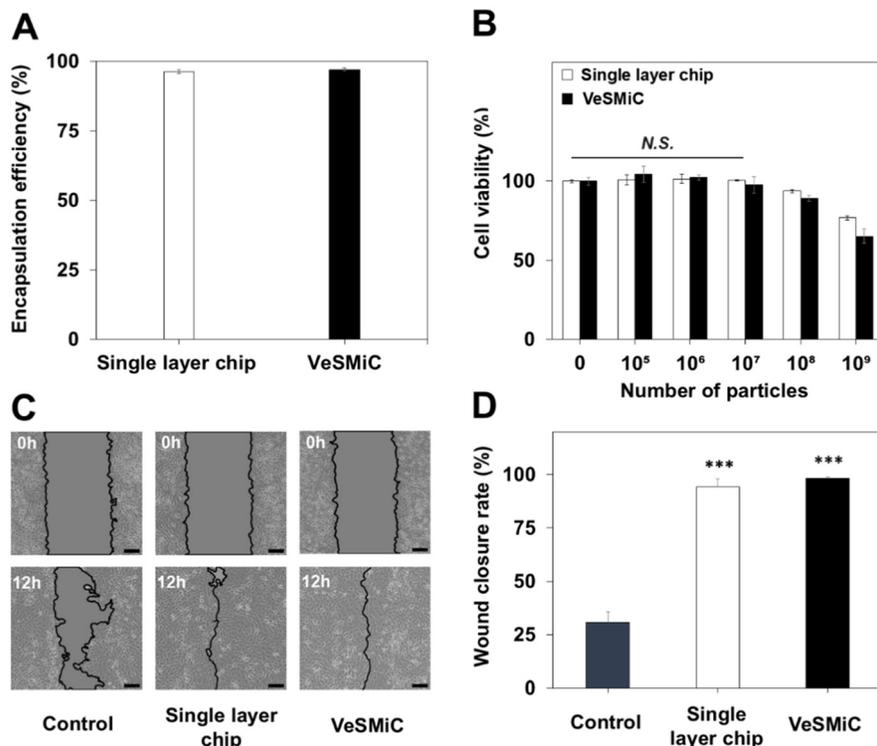
Fig. 5 (A) Comparative analysis of nucleic acid EE% for the single layer chip and the tapered inlet structures of VeSMiC, evaluated under their respective optimal production conditions (4 mL min^{-1}, 16 mL min^{-1}). (B) Cytotoxicity evaluation of LNPs, with cell viability assessed as a function of LNP particle concentration. (C) Representative images of the wound healing assay. Cells were observed at 0 and 12 hours after treatment with PBS (control), LNPs produced by the single layer chip, and the tapered inlet structure VeSMiC. (D) Quantitative analysis of the wound closure rate of HaCaT cells for each group (***; $P < 0.001$, extremely significant).

excellent therapeutic potential in an *in vitro* model. Collectively, these results highlight the promise of the VeSMiC platform for high-throughput production of LNPs without compromising formulation quality or biological performance.

4. Conclusions

In this study, we developed and validated a vertically stacked microfluidic chip that overcomes the critical throughput limitations of conventional LNP production systems. Transitioning PDMS to a polycarbonate-based platform enabled high mixing efficiency and uniform LNP formation under flow conditions. To support stacking, we introduced a tapered inlet that balanced the flow across layers and applied a bonding method capable of withstanding elevated pressures to allow stable high-rate synthesis within the VeSMiC. The VeSMiC with five stacked layers achieved a 7-fold increase in production rate over a single-layer chip while consistently generating LNPs with preserved quality, maintaining a stable PDI below 0.12 and an encapsulation efficiency exceeding 96%. The resulting LNPs also retained therapeutic activity in an *in vitro* wound-healing model. Theoretical analysis also suggests that parallel expansion of VeSMiC can increase throughput by several orders of magnitude, highlighting its scalability for large-volume LNP

manufacturing. Together, the scalable hydraulic design and preserved nanoparticle quality position this platform as a strong candidate for future integration into clinical nucleic acid therapeutics production pipelines.

Author contributions

Zhaoyu Zhang: conceptualization, methodology, validation, investigation, writing – original draft preparation, writing – review and editing, and visualization; Jaejeung Kim: conceptualization, methodology, validation, investigation, writing – review and editing, and visualization; Jinwoo Hwang: validation and investigation; Hyunjo Seo: validation and investigation; Geonha Kim: validation and investigation; Kyung-A Hyun: methodology, validation, and investigation; Seoyeon Choi: conceptualization, methodology, and visualization; Hyo-Il Jung: conceptualization, supervision, and project administration.

Conflicts of interest

The authors declare the following competing financial interest: Jaejeung Kim and Seoyeon Choi are employees of The DABOM Inc., and Hyo-Il Jung is the founder of the company.

Data availability

The authors confirm that the data supporting the findings of this study are available within the main article and supplementary information (SI). SI includes information regarding microfluidic chip surface treatments, characteristics of LNPs, simulated pressure drops for different inlets, and chip bonding techniques. See DOI: https://doi.org/10.1039/d5lc01130b.

The author will also provide relevant details if there are other reasonable requests.

Acknowledgements

References

1 I. K. Kwon, S. C. Lee, B. Han and K. Park, *J. Controlled Release*, 2012, **164**, 108–114.

2 T. J. Anchordoquy, Y. Barenholz, D. Boraschi, M. Chorny, P. Decuzzi, M. A. Dobrovolskaia, Z. S. Farhangrazi, D. Farrell, A. Gabizon, H. Ghandehari, B. Godin, N. M. La-Beck, J. Ljubimova, S. M. Moghimi, L. Pagliaro, J.-H. Park, D. Peer, E. Ruoslahti, N. J. Serkova and D. Simberg, *ACS Nano*, 2017, **11**, 12–18.

3 R. M. Pearson, V. V. Juettner and S. Hong, *Front. Chem.*, 2014, **2**, 108.

4 Y. K. Jo and D. Lee, *Small*, 2020, **16**, 1903736.

5 M. M. Żak and L. Zangi, *Pharmaceutics*, 2021, **13**, 1675.

6 J. A. Kulkarni, D. Witzigmann, J. Leung, Y. Y. C. Tam and P. R. Cullis, *Nanoscale*, 2019, **11**, 21733–21739.

7 N. Pardi, M. J. Hogan, F. W. Porter and D. Weissman, *Nat. Rev. Drug Discovery*, 2018, **17**, 261–279.

8 J. Yan, D. D. Kang, C. Wang, X. Hou, S. Du, S. Wang, Y. Xue, Z. Liu, Y. Li, Y. Zhong, B. Deng, D. W. McComb and Y. Dong, *Nano Res.*, 2024, **17**, 9095–9102.

9 A. R. Ferhan, S. Park, H. Park, H. Tae, J. A. Jackman and N. Cho, *Adv. Funct. Mater.*, 2022, **32**, 2203669.

10 N. Warne, M. Ruesch, P. Siwik, P. Mensah, J. Ludwig, M. Hripcsak, R. Godavarti, A. Prigodich and M. Dolsten, *Nat. Biotechnol.*, 2023, **41**, 183–188.

11 R. Gao, Z. Lv, Y. Mao, L. Yu, X. Bi, S. Xu, J. Cui and Y. Wu, *ACS Sens.*, 2019, **4**, 938–943.

12 A. A. S. Bhagat, H. Bow, H. W. Hou, S. J. Tan, J. Han and C. T. Lim, *Med. Biol. Eng. Comput.*, 2010, **48**, 999–1014.

13 S. Kalyan, C. Torabi, H. Khoo, H. W. Sung, S.-E. Choi, W. Wang, B. Treutler, D. Kim and S. C. Hur, *Micromachines*, 2021, **12**, 257.

14 M. Maeki, S. Uno, A. Niwa, Y. Okada and M. Tokeshi, *J. Controlled Release*, 2022, **344**, 80–96.

15 N. Kimura, M. Maeki, Y. Sato, Y. Note, A. Ishida, H. Tani, H. Harashima and M. Tokeshi, *ACS Omega*, 2018, **3**, 5044–5051.

16 J. Kotouček, F. Hubatka, J. Mašek, P. Kulich, K. Velínská, J. Bezděková, M. Fojtíková, E. Bartheldyová, A. Tomečková, J. Stráská, D. Hrebík, S. Macaulay, I. Kratochvílová, M. Raška and J. Turánek, *Sci. Rep.*, 2020, **10**, 5595.

17 J. Kim, D. H. Lee, H. Seo, H. Lee, G. Kim, C. Nie, Y. Hong, Y. Yoon, J. Lim, S. J. Park, J. Y. Yang, S. Choi, S. Park and H. Jung, *Small*, 2025, e06162.

18 S. J. Shepherd, X. Han, A. J. Mukalel, R. El-Mayta, A. S. Thatte, J. Wu, M. S. Padilla, M.-G. Alameh, N. Srikumar, D. Lee, D. Weissman, D. Issadore and M. J. Mitchell, *Proc. Natl. Acad. Sci. U. S. A.*, 2023, **120**, e2303567120.

19 S. Mehraji and D. L. DeVoe, *Lab Chip*, 2024, **24**, 1154–1174.

20 S. Athey, J. C. Castillo, E. Chaudhuri, M. Kremer, A. Simoes Gomes and C. M. Snyder, *Oxf. Rev. Econ. Policy*, 2022, **38**, 742–770.

21 Z. Kis, C. Kontoravdi, R. Shattock and N. Shah, *Vaccines*, 2020, **9**, 3.

22 J. Y. Han, J. N. La Fiandra and D. L. DeVoe, *Nat. Commun.*, 2022, **13**, 6997.

23 S. J. Shepherd, C. C. Warzecha, S. Yadavali, R. El-Mayta, M.-G. Alameh, L. Wang, D. Weissman, J. M. Wilson, D. Issadore and M. J. Mitchell, *Nano Lett.*, 2021, **21**, 5671–5680.

24 C. Zhu, N. Roa, E. Neathery, N. Parker, J. Delarosa, S. Knackstedt, K. Lee and M. Lal, *Vaccine: X*, 2026, **28**, 100771.

25 S. Clarke, I. Johnston, A. Braun, R. Young, M. Kerin, D. Singh, B. MacDougall, B. Ma, A. Lazic, L. Yee, C. Robin, F. Yuen, P. Harvie and S. Abraham, *Cytotherapy*, 2024, **26**, S147.

26 T. Han, L. Zhang, H. Xu and J. Xuan, *Chem. Eng. J.*, 2017, **326**, 765–773.

27 H. Shan, Q. Lin, D. Wang, X. Sun, B. Quan, X. Chen and Z. Chen, *Front. Bioeng. Biotechnol.*, 2021, **9**, 773705.

28 A. Giorello, A. Nicastro and C. L. A. Berli, *Adv. Mater. Technol.*, 2022, **7**, 2101588.

29 S. J. Shepherd, D. Issadore and M. J. Mitchell, *Biomaterials*, 2021, **274**, 120826.

30 H. Aghaei and A. R. Solaimany Nazar, *Ind. Eng. Chem. Res.*, 2019, **58**, 23032–23045.

31 K.-I. Min, D. J. Im, H.-J. Lee and D.-P. Kim, *Lab Chip*, 2014, **14**, 3987–3992.

32 S. Gimondi, H. Ferreira, R. L. Reis and N. M. Neves, *ACS Nano*, 2023, **17**, 14205–14228.

33 D. Jung, S. Jang, D. Park, N. H. Bae, C. S. Han, S. Ryu, E.-K. Lim and K. G. Lee, *BioChip J.*, 2025, **19**, 79–90.

34 J. Di, Y. Xu and T. Li, *Asian J. Pharm. Sci.*, 2025, 101092.

35 M. Maeki, Y. Okada, S. Uno, K. Sugiura, Y. Suzuki, K. Okuda, Y. Sato, M. Ando, H. Yamazaki, M. Takeuchi, A. Ishida, H. Tani, H. Harashima and M. Tokeshi, *Appl. Mater. Today*, 2023, **31**, 101754.

36 C. Nie, H. Jeong, K.-A. Hyun, S. Park and H.-I. Jung, *Analyst*, 2024, **149**, 4072–4081.

37 K. A. Vijayalakshmi, M. Mekala, C. P. Yoganand and K. Navaneetha Pandiyaraj, *Int. J. Phys. Sci.*, 2012, 7(15), 2264–2273.

38 J. Kelar, M. Shekargoftar, R. Krumpolec and T. Homola, *Polym. Test.*, 2018, **67**, 428–434.

39 M. Jang, C. K. Park and N. Y. Lee, *Sens. Actuators, B*, 2014, **193**, 599–607.

40 J. Wang, N. Zhang, J. Chen, V. G. J. Rodgers, P. Brisk and W. H. Grover, *Lab Chip*, 2019, **19**, 3618–3627.

41 M. N. O'Brien Laramy, A. P. Costa, Y. M. Cebrero, J. Joseph, A. Sarode, N. Zang, L. J. Kim, K. Hofmann, S. Wang, A. Goyon, S. G. Koenig, M. Hammel and G. L. Hura, *Mol. Pharmaceutics*, 2023, **20**, 4285–4296.

42 S. Park, Y.-J. Yoon, Y. Hong, J. Yu, J.-M. Cho, Y. J. Jeong, H. Yu, H. Jeong, H. Lee, S. Hwang, W.-G. Koh, J. Y. Yang, K.-A. Hyun, H.-I. Jung and J.-Y. Lim, *Bioact. Mater.*, 2025, **47**, 229–247.

43 A. Lai, N. Altemose, J. A. White and A. M. Streets, *J. Micromech. Microeng.*, 2019, **29**, 107001.

44 Y. Liao, Y. Mechulam and B. Lassalle-Kaiser, *Sci. Rep.*, 2021, **11**, 20119.

45 R. S. Fernandes, G. De Assis Burle-Caldas, S. A. R. Sergio, A. F. Bráz, N. P. Da Silva Leite, M. Pereira, J. De Oliveira Silva, N. S. Hojo-Souza, B. De Oliveira, A. P. S. M. Fernandes, F. G. Da Fonseca, R. T. Gazzinelli, D. Dos Santos Ferreira and S. M. R. Teixeira, *J. Nanobiotechnol.*, 2025, **23**, 221.

46 M. Maeki, Y. Fujishima, Y. Sato, T. Yasui, N. Kaji, A. Ishida, H. Tani, Y. Baba, H. Harashima and M. Tokeshi, *PLoS One*, 2017, **12**, e0187962.

47 I. Pereiro, A. Fomitcheva Khartchenko, L. Petrini and G. V. Kaigala, *Lab Chip*, 2019, **19**, 2296–2314.

48 M. N. O. Laramy, A. P. Costa, Y. M. Cebrero, J. Joseph, A. Sarode, N. Zang, L. J. Kim, K. Hofmann, S. Wang, A. Goyon, S. G. Koenig, M. Hammel and G. L. Hura, *Mol. Pharmaceutics*, 2023, **20**(8), 4285–4296.

49 N. Minocha and J. B. Joshi, *Int. J. Heat Mass Transfer*, 2020, **151**, 119420.

50 R. Tarodiya and B. K. Gandhi, *Adv. Powder Technol.*, 2020, **31**, 4751–4767.

51 D. S. Jang, S. H. Ham, H. H. Shin and Y. Kim, *Appl. Therm. Eng.*, 2024, **237**, 121799.

52 M. N. O'Brien Laramy, A. P. Costa, Y. M. Cebrero, J. Joseph, A. Sarode, N. Zang, L. J. Kim, K. Hofmann, S. Wang, A. Goyon, S. G. Koenig, M. Hammel and G. L. Hura, *Mol. Pharmaceutics*, 2023, **20**, 4285–4296.